AGU PUBLICATIONS

JGR

Journal of Geophysical Research: Oceans

RESEARCH ARTICLE

10.1002/2015JC011296

Special Section:
Forum for Arctic Modeling and Observing Synthesis (FAMOS): Results and Synthesis of Coordinated Experiments

Dynamics of an idealized Beaufort Gyre: 1. The effect of a small beta and lack of western boundaries

Jiayan Yang[1], Andrey Proshutinsky[1], and Xiaopei Lin[2]

[1]Department of Physical Oceanography, Woods Hole Oceanographic Institution, Woods Hole, Massachusetts, USA, [2]Key Laboratory of Physical Oceanography, Ocean University of China, Qingdao, China

Abstract The Beaufort Gyre in the Arctic Ocean differs from a typical moderate-latitude gyre in some major aspects of its dynamics. First, it is located in a basin without a western boundary, which is essential for closing midlatitude circulations. Second, the gradient in Coriolis parameter, β, is small and so the validity of the Sverdrup balance is uncertain. In this paper, we use an idealized two-layer model to examine several processes that are related to these two issues. In a circular basin with closed geostrophic contours in interior, the variability of vorticity in the upper layer is dominated by eddies. But in the time-mean circulation, the main dynamical balance in the basin's interior is between the curl of wind stress and the eddy vorticity fluxes. The torque of friction becomes important along the boundary where the rim current is strong. It is found that the smallness of β has only a relatively small impact in a circular basin without a meridional boundary. The gyre is considerably more sensitive to the existence of a meridional boundary. The time-mean circulation weakens considerably when a peninsula is inserted between the model's center and the rim. (One side of the peninsula is dynamically equivalent to a midlatitude western boundary.) The gyre's sensitivity to β has also increased significantly when a meridional boundary is present. Subsurface ridges have similar effects on the gyre as a boundary, indicating that such topographic features may substitute, to some extents, the dynamical role of a western boundary.

Key Points:
- The BG differs from midlatitude typical gyres because of small beta and absence of western boundary
- Eddies play a leading role in the main balances of dynamics and volume fluxes
- Topographic effect is significant and also elevates the beta effect

Correspondence to:
J. Yang,
jyang@whoi.edu

Citation:
Yang, J., A. Proshutinsky, and X. Lin (2016), Dynamics of an idealized Beaufort Gyre: 1. The effect of a small beta and lack of western boundaries, *J. Geophys. Res. Oceans*, *121*, 1249–1261, doi:10.1002/2015JC011296.

Received 3 SEP 2015
Accepted 19 DEC 2015
Accepted article online 26 DEC 2015
Published online 12 FEB 2016

1. Introduction

The Beaufort Gyre (BG) is an anticyclonic circulation of sea ice and water in the Arctic Canada Basin. It is forced primarily by an anticyclonic wind stress that is associated with the Beaufort High (BH)—a high sea level pressure (SLP) over the Beaufort Sea (Figure 1). The BG plays a pivotal role in the global climate system. A large amount of fresh water (FW), a combination of sea ice and a low-salinity water mass, is stored in the Beaufort Sea (BS). This FW reservoir is a main source for the southward FW flux to the Nordic Seas and to the Subpolar North Atlantic Ocean where the North Atlantic Deep Water (NADW) is formed. The NADW formation, which is a primary driver of the Atlantic Meridional Overturning Circulation (AMOC), is sensitive to changes in the FW flux from the Arctic Ocean and thus to the FW content (FWC) in the BG [*Dickson et al.*, 1988; *Proshutinsky et al.*, 2002; *Curry and Mauritzen*, 2005]. Observations have shown that the FWC in the BG has increased dramatically since the 1990s and has reached an alarming high level [*Proshutinsky et al.*, 2009, 2013; *McPhee et al.*, 2009; *Morison et al.*, 2012; *Giles et al.*, 2012]. The increase in BG FWC has been accompanied by an increase in the convergence of the surface Ekman transport [*Yang*, 2009; *Proshutinsky et al.*, 2009]. The rapid buildup of the FWC in the last two decades could affect the stability of the AMOC. The key to understanding the FWC in the Beaufort Sea and its variability is to understand the dynamical processes and balances that govern the Beaufort Gyre and its variability.

The anticyclonic wind stress forces a convergence of the surface low-salinity water toward the center of the Beaufort Sea [*Proshutinsky et al.*, 2002; *Yang*, 2006, 2009]. This convergence and the resultant Ekman pumping (or downwelling) not only drives an anticyclonic BG but also maintains the FWC, i.e., the storage of low-salinity water. So the state of the FWC in the Beaufort Sea is intimately related to the strength of the BG. In fact, the geostrophic transport of the BG has been strengthening along with the FWC increase [*McPhee*, 2013].

The basic dynamics that govern the Beaufort Gyre has not been adequately understood. There are some potentially fundamental differences between the BG and a typical wind-driven gyre, such as the subtropical

gyre in the North Atlantic Ocean. Theories of wind-driven circulations, which have been developed mainly for moderate-latitude oceans that are bounded zonally by an eastern and a western boundary, may not apply to the BG. First, the planetary β (where $\beta = df/dy$ is the meridional gradient of the Coriolis parameter f) is relatively small in the Arctic and so it is unclear whether the Sverdrup relation remains valid as the zeroth-order balance in dynamics. Second, the Arctic Ocean lacks a well-defined western boundary and so it is not obvious how the gyre is closed and where the vorticity flux from wind stress is balanced. We must point out that these two factors, i.e., a small β and a lack of zonal boundaries, are not unique for the Beaufort Gyre. Studies of the Antarctic Circumpolar Current (ACC) would have to deal with similar questions. Results from the ACC study, such as the roles of eddies and topography [*Marshall et al*., 2002; *Marshall and Radko*, 2003], are helpful for understanding the BG dynamics.

The Arctic Ocean circulation is a complex system that involves wind stress and buoyancy forcing, interactions with sea ice and exchanges with the Atlantic and Pacific Oceans. Three dimensional general circulation models have improved considerably and are capable of simulating key features that are consistent with observations (see a review by *Proshutinsky et al*. [2011]). But idealized models continue to play an important role in developing ideas and testing hypotheses. For example, *Yang* [2005] used a one-layer model to show that the sense of the Atlantic water (AW) circulation is strongly influenced by the potential vorticity (PV) fluxes from the Atlantic and Pacific Ocean. This idealized study has motivated some further studies that used more complete three-dimensional models [e.g., *Karcher et al*., 2007]. More recently, *Spall* [2013] showed that eddy fluxes between the boundary current and interior are important drivers for the AW rim current and the existence Arctic halocline. Interestingly, Spall also showed that a BG-like circulation was forced even though the wind stress is spatially uniform (zero curl) in Spall's model. It was the gradient of sea ice velocity that gives rise to a curl of surface stress and drives an anticyclonic gyre in Spall's model. In another idealized modeling study, *Davis et al*. [2014] also demonstrate how changes in sea ice may have affected the curl of net surface stress that is exerted on the ocean and affected the BG strength.

In this study, we will use a simple idealized model to evaluate roles of different factors and to examine key dynamical processes and balances. The model and the forcing are introduced in section 2. This will be followed by discussions of model results in section 3 and summary given in section 4.

2. Model Description

In this study, we employ a two-layer, wind-driven nonlinear oceanic model that was used by *Yang and Pratt* [2013, 2014] and *Yang* [2015] in both idealized and realistic simulations. It is assumed that the Arctic Ocean can be approximated by a two-layer system where the upper layer driven by winds represents the upper relatively low-salinity waters and the second layer with much higher salinity waters represents the Atlantic water layer of the Arctic Ocean. The model is governed by the following set of equations:

$$\begin{aligned}
\frac{d\vec{u}_1}{dt} + f\vec{k}\times\vec{u}_1 &= -g\nabla\eta_1 - A\nabla^4\vec{u}_1 - (1-H(h_2))\vec{F}_1 + \frac{\vec{\tau}_{wind}}{\rho_1 h_1} \\
\frac{d\vec{u}_2}{dt} + f\vec{k}\times\vec{u}_2 &= -g\nabla\left(\eta_1 + \frac{\Delta\rho}{\rho_2}\eta_2\right) - A\nabla^4\vec{u}_2 - \vec{F}_2 + (1-H(h_1))\frac{\vec{\tau}_{wind}}{\rho_2 h_2} \\
\frac{\partial\eta_1}{\partial t} + \nabla\cdot(h_1\vec{u}_1 + h_2\vec{u}_2) &= 0 \\
\frac{\partial\eta_2}{\partial t} + \nabla\cdot(h_2\vec{u}_2) &= 0
\end{aligned} \tag{1}$$

where (u_i, v_i) and h_i are the velocity and layer thickness in the ith layer ($i = 1, 2$ for the upper and lower layers, respectively), η_1 and η_2 are the surface heights for layers 1 and 2 respectively, $\Delta\rho$ =1.0 kg/m^3 is the water density difference between two layers, ρ_1=1025 kg/m^3 and ρ_2=1026 kg/m^3 are the water density in the upper and lower layers, respectively, and ρ_0=1025.875 kg/m^3 is the mean density. In all experiments, we use circular and bowl-shape basins with the maximum depth of 4000 m. The model grid size is 5 km. No normal flow and no-slip conditions are applied along the lateral boundary. $\vec{F}_n = -\lambda|\vec{u}_n|\vec{u}_n/h_n$ is the bottom friction with a bottom drag coefficient $\lambda = 10^{-3}$ m^{-1}. The bottom friction is applied to the layer that is in contact with the bottom. It applies typically to the lower layer only. But in areas where the lower layer has a zero thickness, the bottom friction is applied to the upper layer. This is handled by the Heaviside Step

Function $H(h_i)$ in equation (1) ($H(h_i) = 1$ if $h_i > 0$, and $H(h_i) = 0$ if $h_i \leq 0$). In the deep basin, the lower layer has a large thickness and its velocity is weak in a steady state. So the bottom friction is typically small except in the shelf near the boundary where the water depth is shallow.

The initial condition is a state of rest with layer interface set at the 400 m depth or at the bottom wherever it is shallower than 400 m. The model allows outcropping of the lower layer ($h_1 = 0$) and grounding of the upper layer ($h_2 = 0$). The wind stress is applied to the lower layer wherever it outcrops. The wind stress forcing in outcropped areas is handled by the Heaviside Step Function $H(h_i)$ in equation (1). The model uses a biharmonic mixing parameterization with a horizontal viscosity $A = 10^{11}$ m^4 s^{-1}. Idealized bathymetry and wind forcing are used to conduct a set of numerical experiments to resolve questions formulated above.

A circular bowl-shape basin (Figure 2a) is used in the control run. It has a linear slope of 0.03 off the southern boundary and is flat in the interior. The minimum depth in the model is set at 250 m at the southern boundary. The width of the continental slope is about 125 km. The internal Rossby deformation radius $d = c/f$, where $c = [g(\Delta\rho/\rho_0)h_1h_2/(h_1 + h_2)]^{1/2}$ is the speed of internal shallow-water gravity waves, is about 15–20 km in the interior depending on values of h_1 and h_2, which is somewhat larger than the Arctic Ocean data-based assessed value of about 13 km [*Zhao et al*., 2014].

The model has a spatial resolution of 5 km, which is considered as eddy permitting. A prescribed anticyclonic wind stress (Figure 2b) is used to force the model. Note that the wind stress curl (Figure 2c) is negative with a magnitude of about 10–20 cm/d (Ekman pumping velocity), which is comparable with data-based estimates by *Yang* [2009]. A β-plane is used with the values of β and f set at 85°N. The model's "North Pole" is located at the basin's center where the Coriolis parameter f has the maximum value.

3. Model Results and Analyses

3.1. The Control Run

In the first experiment, referred hereafter as *the control run* (*CTR*), we apply the steady wind stress (Figure 2b) for a period of 20 years. In a relatively small domain (Figure 2a), the circulation reaches an equilibrium state, defined here as a steady 5 year running mean in the upper layer with thickness h_1, within 20 years. Boundary Kelvin waves and planetary and topographic Rossby waves, which are excited by the wind stress, play a central role in the spin-up process as demonstrated by *Luneva et al*. [2012] who use a homogeneous model in a similar circular basin. But the spin-up of the gyre in our model also involves baroclinic waves and eddies.

There is considerable short-term variability that is associated with eddies even when an equilibrium state is reached. This is shown in the time evolution of h_1 at basin's center (Figure 3a). The anticyclonic wind stress forces an offshore Ekman transport toward the basin's center. The thickness of the upper layer increases almost linearly in the first 5 years of the spin-up. The monotonic increase in h_1 at basin's center halts once eddies start to form. The convergence of the Ekman transport is balanced mainly by the residual eddy transport. Friction also induces a divergent ageostrophic transport (it is analogous to the bottom Ekman layer transport except that the friction in the interior is dominated by the lateral friction) (see Part 2 of this paper by *Yang et al*. [2015]). This balance helps the model to establish an equilibrium state.

In its mean field and in a snapshot (Figures 3b and 3c), the upper layer thickness h_1 is zero near the boundary, i.e., the lower layer outcrops. Its thickness increases rapidly offshore across the continental slope where it has the largest gradient. When the shear of the slope current becomes large enough during the spin-up, it becomes baroclinically unstable and eddies are formed consequently. Eddies induce a residual transport, i.e., $-\overline{\nabla \cdot (h_1' \vec{u}_1')}$, in the time-mean continuity equation (where prime and overbar denote eddy and time-mean fields, respectively). This residual transport, which is divergent in this run, plays a leading role in balancing the surface Ekman convergence (see Part 2 of this paper by *Yang et al*. [2015]). This is why the spin-up of the h_1 reaches an equilibrium state as soon as eddies are formed (Figure 3a) [see also *Munday et al*., 2013; *Lique et al*., 2015]. Eddies of various sizes can be identified in Figure 3b, a snapshot of h_1 at the end of the 20 year simulation. The radius of those eddies, which are measured by the sizes of closed geostrophic contours in snapshots of h_1, ranges from 15 km to more than 50 km. This is larger than the internal deformation radius of 15–20 km in the model. As noted in previous studies (see the discussion by *Vallis* [2006]),

the horizontal scale of eddies can be a few times larger than the local deformation radius. Such differences are often due to inverse cascade or to the setting of instability scales.

In the model's time-mean state, the geostrophic velocity in the lower-layer vanishes, i.e., $\nabla\eta_1$ and $\Delta\rho\nabla\eta_2/\rho_2$ cancels each other in (1). The mean state becomes equivalently a one and one-half layer reduced-gravity system. Even though this spun-up state is essentially the same as what is expected from the classic model of *Anderson and Gill* [1975], the spin-up processes could be quite different here due to the absence of a western boundary and planetary Rossby waves. Nevertheless, the surface geostrophic velocity, which is proportional to $\nabla\eta_1$, is also proportional to $-\nabla\eta_2$ or to ∇h_1 when the mean geostrophic velocity in the lower layer becomes zero. The averaged geostrophic velocity between basin's center and the boundary is proportional to the Δh_1, the difference of the upper layer thickness between the center of the gyre and the boundary. We will use Δh_1 as the proxy index to measure the strength of the time-mean transport hereafter.

Due to the divergence of the Ekman transport from the boundary, the upper-layer thickness becomes zero and the low layer outcrops along the boundary within the slope area. The time-averaged h_1 between 15 and 20 year shows that the maximum layer thickness at the center is about 630 m (Figure 3c), an increase of more than 200 m from the initial thickness of 400 m. The h_1 difference between the center and boundary in the time-mean state, is accompanied with an anticyclonic time-mean circulation. In our model, we set the density difference between two layers to be $\Delta\rho$ =1.0 kg/m^3, which is about $\Delta S = 1.3$ if the temperature's contribution to $\Delta\rho$ is small. For the reference salinity of $S_{ref} = 34.8$, the equivalent FWC in the control run would be about 23 m. This is qualitatively similar to what is estimated from observation (Figure 1) [*Timokhov and Tanis*, 1997].

3.2. Dynamical Balance

Due to a small β in polar latitudes and a lack of western boundary, the time-mean BG is probably governed by a set of dynamical balances that are considerably different from those in a moderate-latitude gyre where the Sverdrup balance and frictional WBC dynamics are the zeroth-order dynamics. Here we analyze the time-mean vorticity equation. Cross-differentiating two components in the first equation in (1) yields the vorticity equation for the upper layer, i.e.,

$$\frac{\partial\zeta}{\partial t} = -\nabla\cdot[\vec{u}_1(f+\zeta)] + \vec{k}\cdot\nabla\times\left(\frac{\vec{\tau}_{wind}}{\rho_1 h_1}\right) - \vec{k}\cdot\nabla\times\vec{F}_1 \tag{2}$$

where $\zeta = v_x - u_y$ is the relative vorticity, and $\vec{F}_1$ is the sum of lateral and bottom friction in the upper layer. Equation (2) shows that the vorticity in the upper layer changes in response to divergences of planetary and relative vorticity advection, the curl of depth-averaged wind stress and the torque of friction.

The term balance in (2) at the center of basin for the final 2 years of the 20 year simulation is shown in Figure 4. There is a large variability in each term with a typical time scale of 10–30 days. The amplitude of the vorticity change (black line), i.e., the left-hand side term in (2), is dominated by the nonlinear advection term $-\nabla\cdot(\vec{u}_1\zeta)$ (green line). Other terms have much smaller amplitudes. Variations on such time scales are typically induced by eddies. It is more interesting, however, to analyze the time-mean balance in (2).

We denote each variable as the sum of its time-mean and eddy components, e.g., $\zeta = \zeta_0 + \zeta'$ for the relative vorticity. The following time-mean balance in vorticity fluxes is obtained by averaging equation (2) over a time period that is much longer than a typical time scale associated with eddy variability (about 10–30 days as revealed in Figure 4):

$$0 = -\nabla\cdot[\vec{u}_{10}(f+\zeta_0)] - \overline{\nabla\cdot(\vec{u}_1'\zeta')} + \overline{\vec{k}\cdot\nabla\times\left(\frac{\vec{\tau}_{wind}}{\rho_1 h_1}\right)} - \overline{\vec{k}\cdot\nabla\times\vec{F}_1} \tag{3}$$

where the overbar represents the time averaging.

The mean flow advection of the vorticity, i.e., the first term on the right-hand side is very small. This is not surprising since the planetary β is very small in the control run (which is set at 85°N), and the mean flow in the interior is weak. The balance is mainly among the last three terms, eddy vorticity flux, the curl of wind stress and friction torque. The distribution of each time-mean term is symmetric about the center and thus varies only with the radius $r = \sqrt{x^2+y^2}$. The distributions of the last three terms in (3) are displayed in Figure 5 as a function of the basin's radius r. In the interior region within $r \le 300$ km, the curl of the depth-

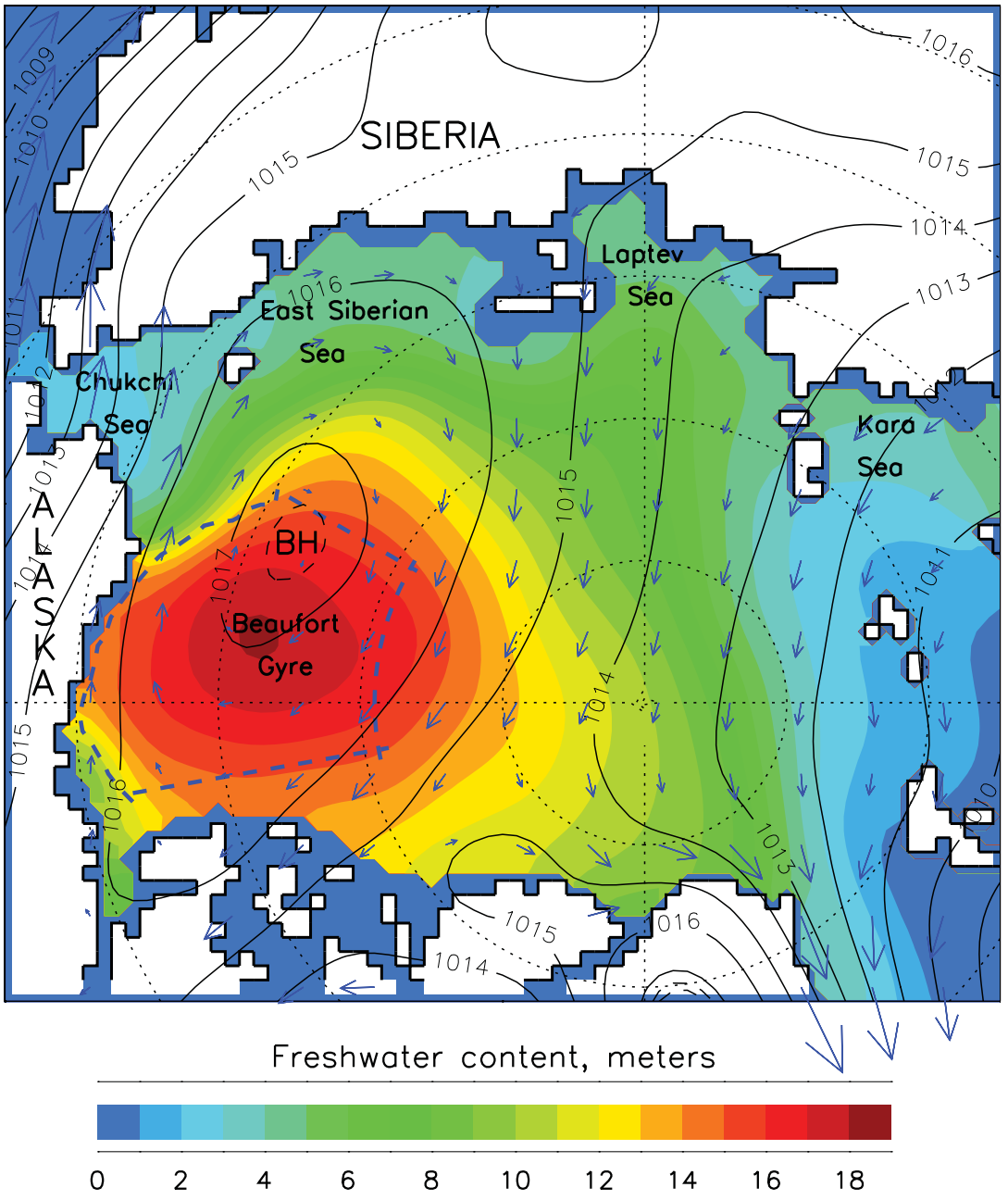

Figure 1. Climatological (all seasons mean 1950–1980) freshwater content (m) in the BG region calculated relatively 34.8 reference salinity based on the Environmental Working Group Atlas of the Arctic Ocean salinity data [*Timokhov and Tanis*, 1997]. Solid black lines depict sea level pressure (SLP, hPa) averaged for the same period. BH stands for Beaufort High and shows location of the BH maximum SLP. Black and blue arrows indicate wind and Ekman transport vectors, respectively.

averaged wind stress (red line) is a leading term, and is mainly balanced by the eddy vorticity flux term (black line). The curl of the depth-averaged wind stress increases rapidly toward the southern rim. This is mainly due to the thinning of the upper layer. In the areas where $r \geq 400$ km, the curl of wind stress is mainly balanced by the torque of friction (blue line). It is interesting to note that there is a large eddy flux of vorticity between $r = 300$ and 400 km, indicating strong vorticity flux between the boundary current and the interior by eddies.

In summary, the main balance of dynamics in the interior is between wind stress curl and eddy PV flux, while along the basin's boundary it is among the eddy flux, wind stress curl, and friction torque. The friction is large along the boundary where the layer is thin.

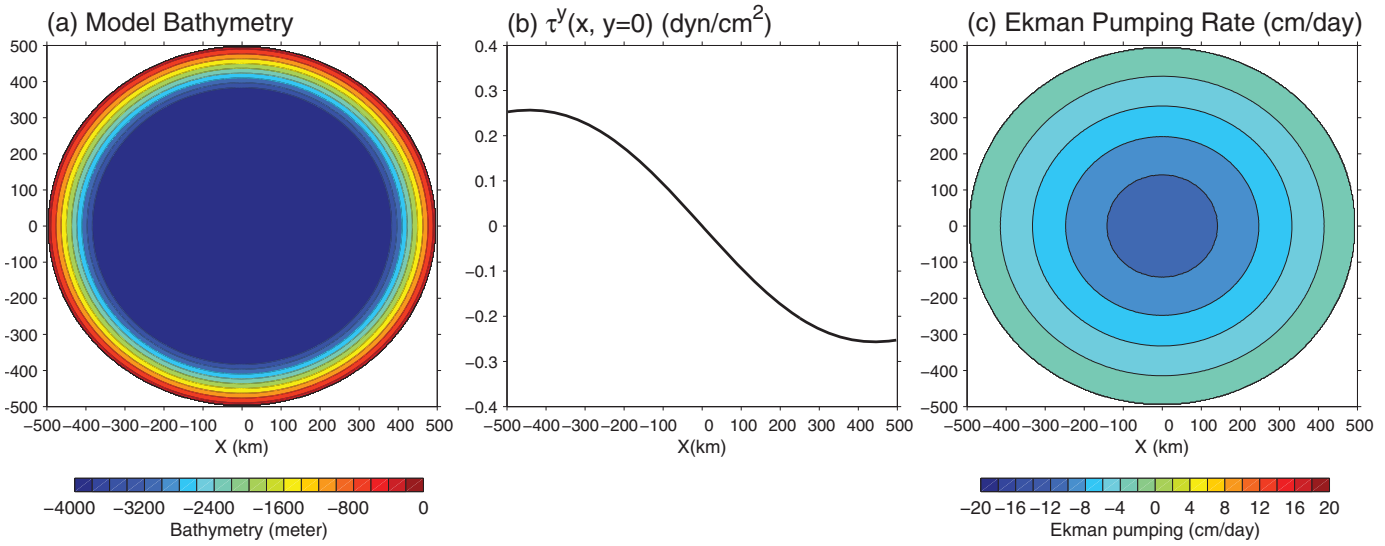

Figure 2. (a) The basin bathymetry for the control model run; (b) the wind stress profile over the basin at $y = 0$; and (c) the Ekman pumping rate (vertical Ekman velocity) $w_e = (1/\rho_0)\vec{k} \cdot \nabla \times (\vec{\tau}_{wind}/f)$.

3.3. Planetary β Effect

The BG is located approximately between 75°N and 85°N and the planetary β is considerably smaller than that in a typical moderate-latitude gyre. As noted earlier, the value of β at 85°N is about one-fifth of that at 35°N (a subtropical gyre) and about one-third of that at 55°N (a subpolar gyre). Our results (Figure 5) show that it is the eddy flux of vorticity, instead of the βv term, that balances the wind stress forcing in the interior. Here we seek to examine whether this dynamical balance in the interior is attributable to the small value of β in BG's high-latitude location or to the basin's bathymetry. Since we already use a small β set at 85°N, which is denoted here as β_{85N}, in the control run, here we conduct an additional experiment by setting β at 40°N, which is referred as β_{40N}. All other parameters, including the Coriolis parameter f_0, remained the same as in the control run. (The reason for not changing f_0 is to keep the internal deformation radius, which is a fundamental scale for eddies, the same as in previous experiments.) Figures 6a and 6b show a snapshot and the time-mean distribution of h_1. Both fields of h_1 are quite similar to that in the control run

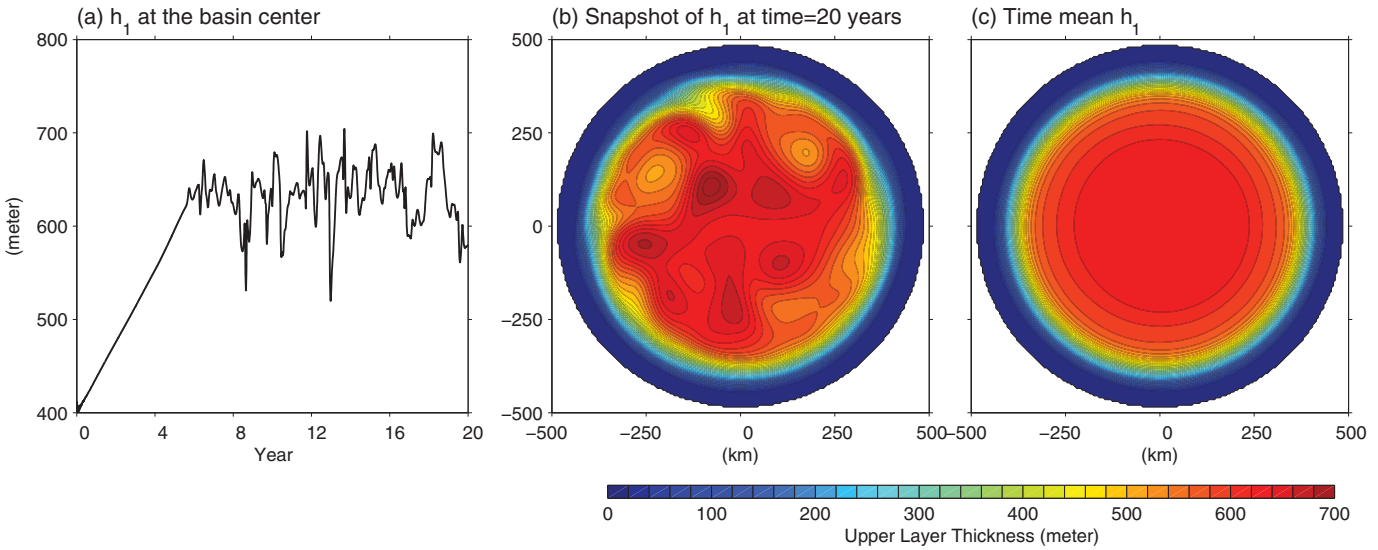

Figure 3. (a) The time evolution of the upper layer thickness h_1 at the center of the basin; (b) the snapshot of h_1 at the end of 20 year simulation; and (c) the time-mean h_1 (averaged in the last 5 years of the 20 year simulation).

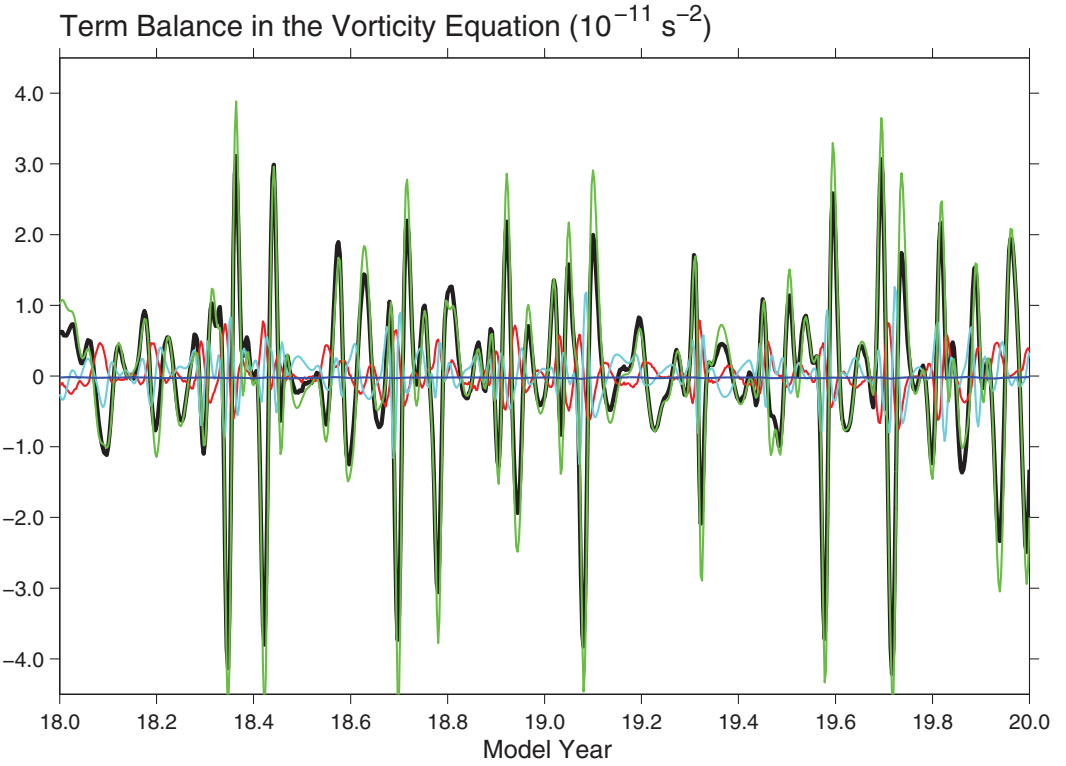

Figure 4. The time evolution of the vorticity balance, i.e., equation (2), in the last 2 years of the 20 year spin-up in the control run. The time derivative of ζ (the left-hand side term, black line), the planetary vorticity advection (the first RHS term, red), the relative vorticity advection (the second RHS term, green), the curl of depth-averaged wind stress (the third RHS term, blue), and the torque of friction (the fourth term on RHS, cyan). The change of the vorticity (black) is clearly dominated by the nonlinear term, i.e., the advection of relative vorticity (green). This suggests the dominance of eddies in the vorticity balance.

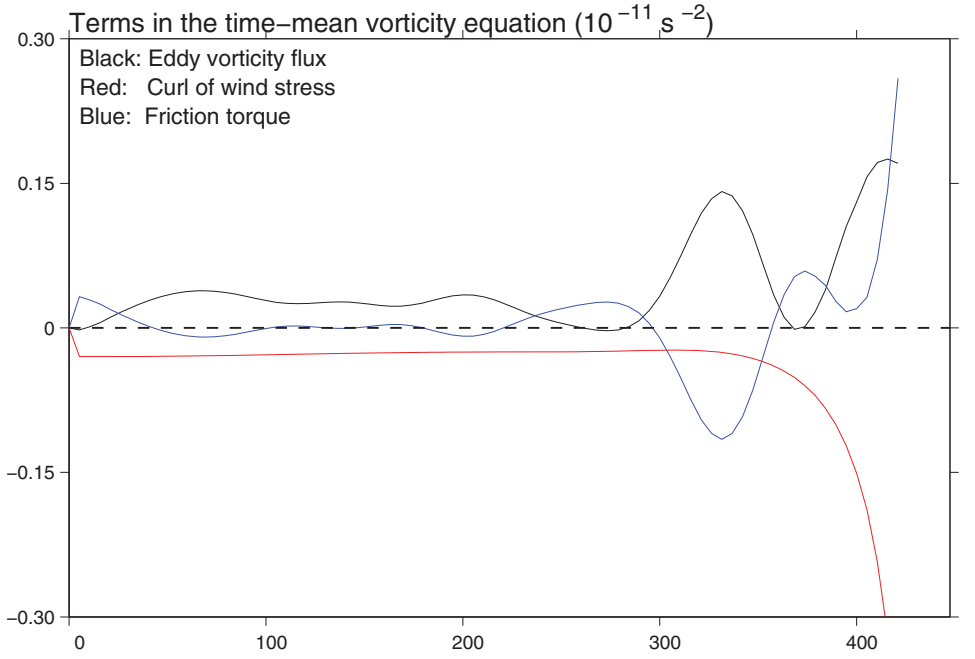

Figure 5. The last three terms in the time-mean vorticity equation (3) between $x = 0$ and $x = 500$ km at $y = 0$. The mean advection of vorticity, i.e., the first term in (3) is very small. In the interior, the main balance is between the eddy vorticity flux and the wind stress curl. Along the boundary, the friction and curl are the main terms providing the balance of water circulation at steady state conditions. The friction is large along the southern boundary where the layer thickness is thin and eddies are suppressed (Figures 3 and 4).

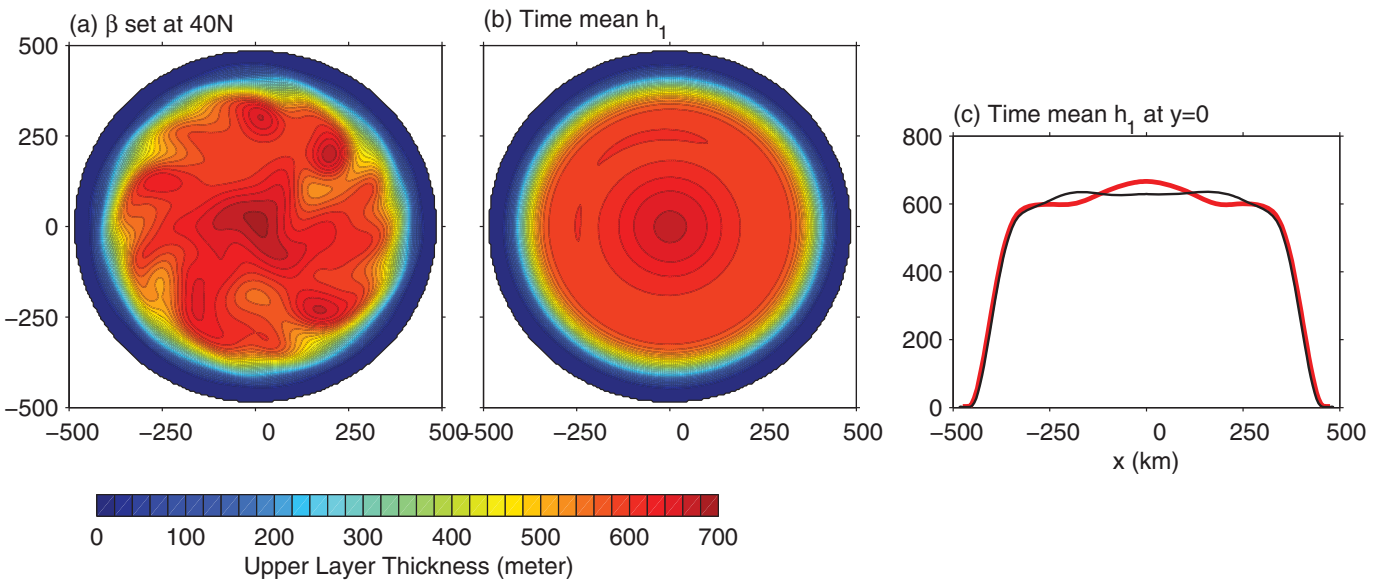

Figure 6. The upper layer thickness h_1 from an experiment that uses the value of β set at 40°N. Everything else remains the same as in the control run. (a) The snapshot of h_1 at the end of 20 year simulation; and (b) the time-mean h_1 (between 16 and 20 year); and (c) the cross-basin profiles of the time-mean h_1 (the red line from the present experiment and the black line from the control run). Note that the change of β does not change the gyre structure qualitatively.

(Figures 3b and 3c). Eddies are apparently present in the snapshots of h_1 in both runs. Like in the control run, the lower layer outcrops along the continental slope, and h_1 fluctuates between 600 and 700 m in the interior due to eddies (Figure 6b).

Figure 6c compares the profiles of the time-mean h_1 across the basin at $y = 0$ between this experiment (red line) and the control run (black line). The mean thickness profiles are nearly identical along the rim. There is, however, a noticeable difference of h_1 in the interior between the control run with β_{85N} (black line) and the current run that uses β_{40N} (red line). In the control run (β_{85N}), the upper layer thickness h_1 is nearly flat at about 630 m between $x = -250$ km and $x = 250$ km. But in the current run with β_{40N}, h_1 increases from about 600 m at $x = \pm 250$ km to about 665 m at $x = 0$. This h_1 profile near the center is accompanied by an anticyclonic mean flow. This contrasts with the control run where the mean velocity is very weak in the interior. The geostrophic transport of the time-mean circulation, which is defined as $Q = \int_0^{r_0} (h_1 \frac{g\Delta\rho}{\rho_0} \frac{\partial h_1}{\partial r}) dr$ and is therefore proportional to Δh_1^2, is about 10% higher than that in the control run.

The change of β would certainly affect the dynamics. But we do not fully understand how this change is related to difference of h_1 between Figures 3c and 6b. We speculate that the difference is due to changes in background vorticity. In the quasigeostropic (QG) dynamics, anticyclonic circulation around closed geostrophic contours (i.e., closed isolines of f/h_1) is typically formed under a negative wind stress curl. A larger β would promote the existence of closed geostrophic contours around the basin's center. This potentially could lead to a more robust geostrophic circulation around the center. A poleward increase in h_1 is needed to accompany an anticyclonic circulation. But this speculation requires a further investigation.

3.4. A Role of a Western Boundary

It was shown that both the time-mean and instantaneous fields of h_1 in a bowl-shape basin, shown in Figure 2a, are not sensitive to β (except a small change of the time-mean h_1 in the interior). This is different from what one would expect from the Sverdrup balance. The primary effect of β on a steady gyre is through the western boundary intensification of the circulation [*Stommel*, 1948]. Therefore, β cannot play its full role in a circular basin without a western boundary. In the next two experiments, we will continue to use an idealized basin but with addition of a western boundary. A wall is inserted between the southern boundary and the basin's center (Figure 7a). The bottom slope around this wall is kept the same as that along the southern boundary, which is 0.03. Two experiments will be discussed, one with β set at 85°N as in the control run and the other at 40°N as the run shown in Figure 6. All model parameters and the surface forcing remain the same as that in the control run.

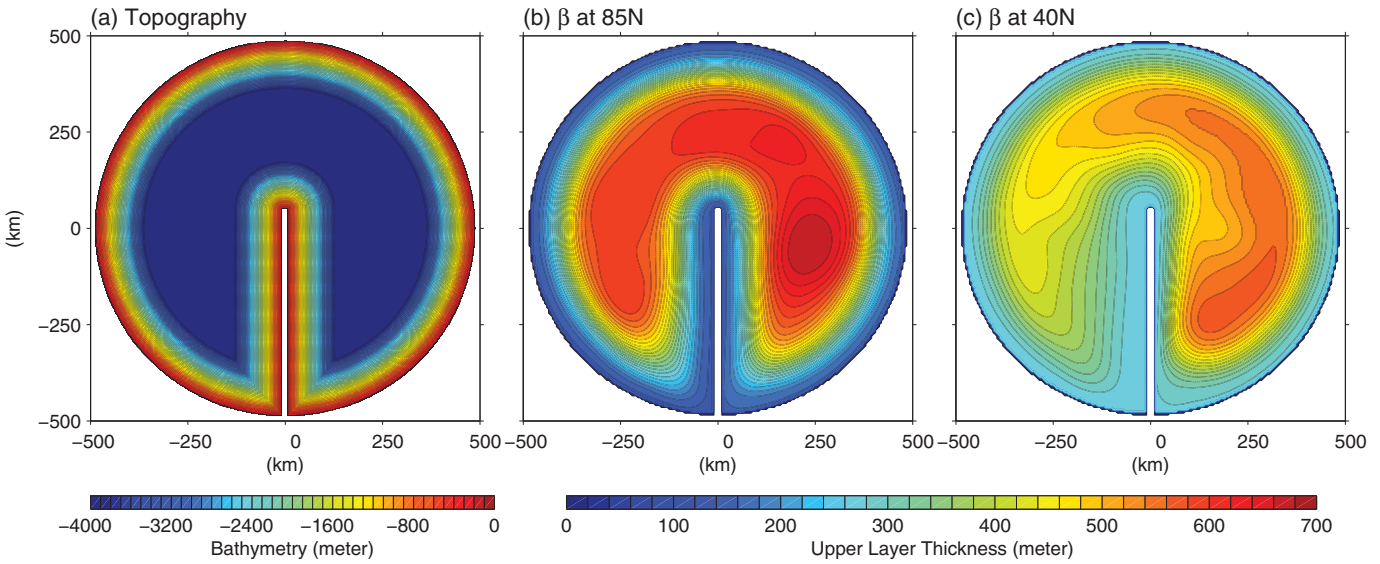

Figure 7. (a) A model bathymetry that includes a western boundary between the basin's center and the southern boundary (the slope of this inserted boundary is the same as that along the southern boundary); (b) the time-mean h_1 from a simulation where β is set at 85°N (the same as the control run). The difference of the upper layer thickness between the center and the boundary, Δh_1, is considerably smaller than that in the control run since the inserted boundary provides a route for shoreward transport that can effectively counter the offshore Ekman transport; and (c) the time-mean h_1 when β is set at 40°N, which shows that the Δh_1 is much reduced compared with Figure 7b. This contrasts with the cases without a western boundary where a change of β has only a small impact on Δh_1.

There are two qualitative changes that are resulted from the insertion of such a western boundary. First, there is a new time scale for the spin-up—the time scale that the WBC is established. The spin-up time scale for the WBC to reach the equilibrium state in the model is considerably longer than the spin-up time scale in the control run shown in Figure 3a. We decide to run model over a longer period, 50 years here, for the spin-up. Second, the model is no longer symmetrical due to Rossby wave propagation. The planetary Rossby waves travels anticyclonically, i.e., in a direction with a higher planetary vorticity f on the right-hand side in the northern hemisphere. So the right-hand side of the inserted boundary is the dynamically western boundary and the left-hand side is the eastern boundary.

The time-mean h_1, averaged between the 45 and the 50 year, are shown in Figure 7b (β_{85N}) and Figure 7c (β_{40N}). In the first case with β_{85N}, the thickness in the gyre's center is about 705 m, which is greater than 630 m in the control run with the same β_{85N}. But the lower layer no longer outcrops in the slope areas in the present run with a western boundary. The minimum h_1 in the time-mean field is about 205 m along the boundary in the slope area. That makes Δh_1, the layer thickness difference between the gyre center and the boundary, about 500 m, which is about 20% less than that in the control run. The geostrophic transport of the gyre, which is proportional to Δh_1^2, is only about 60% of that in the control run.

The presence of the meridional boundary provides a convenient route for shoreward return flow and helps balancing the offshore Ekman transport. The inserted boundary disrupts the circumpolar flow along the southern boundary. Consequently, the southern boundary current is considerably weaker, and the isopycnal slope becomes flatter. The southern boundary current is baroclinically more stable. In fact, the eddy field, which is measured by the eddy kinetic energy distribution, is considerably weaker than that in the control run. The inserted boundary also allows the water mass that is being pushed toward the basin's center by the Ekman transport to return southward, and this is why the layer thickness difference between the basin's center and the rim is much smaller than that in the control run. It should be noted that the shoreward flow is along the "eastern" side (the left side) of the inserted boundary. But the boundary current is stronger on the western (right) side especially in Figure 7c where the β is large (to be discussed next).

Would the presence of the western boundary elevate the impact of β on the gyre? To examine this, we repeat the above experiment with only one change—changing β from β_{85N} to β_{40N}. All other parameters, including the Coriolis parameter f_0 (which set the deformation radius), remain the same as in the previous experiment. The distribution of h_1 (Figure 7c) shows that the layer thickness is about 530 m in the gyre

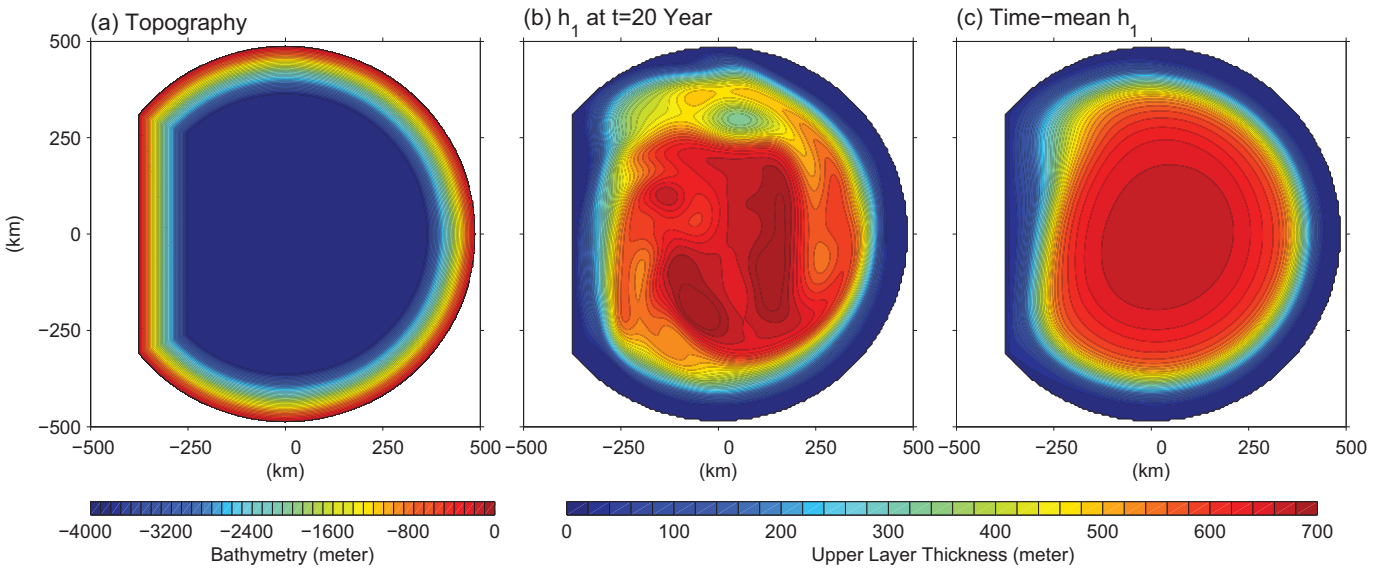

Figure 8. The southern boundary of the Beaufort Sea is not along a parallel, i.e., a line of constant latitude. This experiment is designed to examine whether a southern boundary that extends across latitudes could affect substitute a western boundary. (a) Model bathymetry, (b) a snapshot of h_1 at the end of 20 year simulation, and (c) the time-mean h_1. The results indicate that the effects of such a boundary has little impact on the magnitude of Δh_1.

center and about 230 m at the boundary (Figure 7c). So the difference between the interior and the boundary, Δh_1, is about 300 m, which is about 40% smaller than the previous experiment using β_{85N} (Figure 7b). The geostrophic transport of the gyre is only about 35% of that with β_{85N}.

We will like to point out two interesting differences when compared with the previous set of experiments that have no western boundary. First, the mean geostrophic velocity and its transport strengthen when β increases from β_{85N} to β_{40N} in a bowl-shape basin without a western boundary (Figures 3 and 6). The response and sensitivity to the value of β change when a meridional boundary is inserted, i.e., the gyre weakens substantially when β changes from β_{85N} to β_{40N} (Figures 7b and 7c). Second, the pattern and transport of the time-mean circulation in basin with an inserted boundary are rather insensitive to β. The mean geostrophic transport differs by only about 10% between two experiments that use β_{85N} and β_{40N}, respectively. The effect of β on the geostrophic transport, however, increases significantly when a western boundary is inserted. The mean transport of the gyre is almost a factor of 3 stronger in the experiment using β_{85N} than that with β_{40N}. So the effects of β and the western boundary on the Beaufort Gyre cannot be separated.

The Arctic Beaufort Basin is neither a bowl-shape basin nor a basin with an inserted western boundary (Figure 1). The southern boundary is not along a parallel, i.e., a line of constant latitude. Could a meridionally slanted boundary substitute a western boundary? We conducted another experiment to examine this prospect by using a model bathymetry that is shown in Figure 8a. We ran an experiment with parameters and forcing field that are the same as that in the control run over the overlapped ocean areas. The snapshot of h_1 (Figure 8b) at the end of the 20 year run shows a feature that is qualitatively similar to that in the control run (Figure 3b). But the intensity of eddies, as measured by the eddy kinetic energy, is actually weaker than that in the control run. The lower layer outcrops along the boundary in the slope area and eddies fill the interior. The time-mean h_1 (Figure 8c) also shows a pattern qualitatively similar to that in the control run, except that the maximum thickness in the interior is about 670 m. This compares with 630 m in the control run (Figure 3c). The time-mean geostrophic transport is about 13% stronger than the control run. The difference is due to the difference of eddy intensity as we will discuss in part 2 of this paper [*Yang et al*., 2015].

Another prominent topographic feature in the Arctic Ocean is the existence of several major underwater ridges, such as Chukchi Plateau just north of the Chukchi Sea, Mendeleev Ridge, and Alpha Ridge in the western Arctic Ocean where the BG is centered. Further toward the Eurasian Basin there are Lomonosov Ridge and Gakkel Ridge. Some ridges extend only to some distances offshore while others extend cross the basin. *Nøst and Isachsen* [2003] and *Aaboe and Nøst* [2008] used simplified models with stratification and realistic topography, and invoked PV dynamics to obtain velocity fields in a stratified Nordic Seas and Arctic

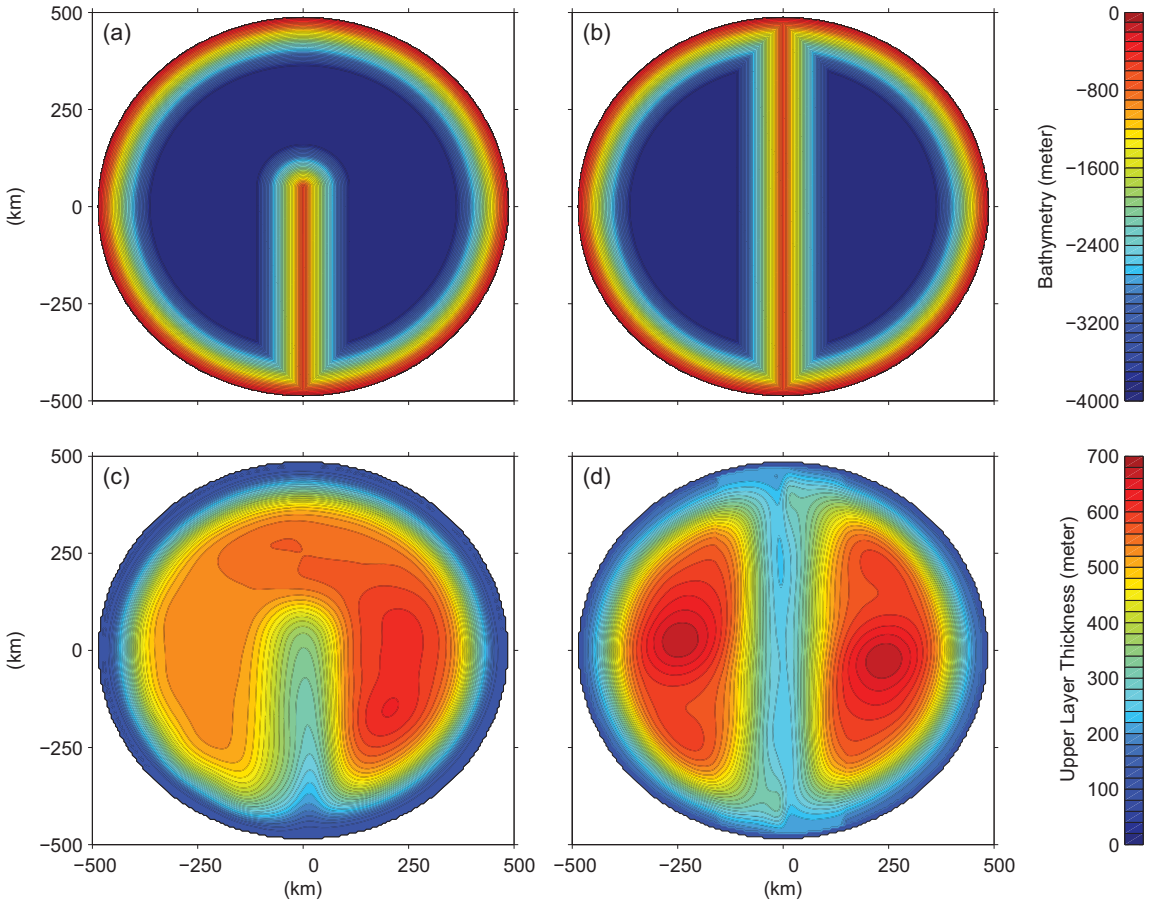

Figure 9. (a and b) Model bathymetries with subsurface ridges. The depth of the ridge crests is 600 m in both experiments. (c and d) The time-mean upper layer thickness h_1 for two experiments that used bathymetries shown in the upper panel. The ridges have considerable impacts on the upper layer circulation, similar to the inserted boundary shown in Figure 7.

Ocean. Their results indicate that the circulation and its long-term variations in the Arctic Mediterranean are strongly influenced by *f*/*h* contours.

We design two additional experiments to examine how such underwater ridges in our idealized model affect the model circulation. The first one has a ridge that extends only half way across the basin (Figure 9a). The crest of the ridge is 600 m below the sea surface. In the second experiment, the ridge, which has the same depth as the previous one, extends across the basin. In either case, the slope of the ridge is the same as the slope along the rim. The same wind stress (Figure 2b) is applied in both experiments. As in the experiments with a western boundary (Figure 7), the model is spun up for a period of 50 years. In the first case, the time-mean h_1 field, averaged in the final 5 years of the spin-up, is actually similar to that with an inserted boundary (Figure 7b). The mean geostrophic flow, which is basically along isolines of h_1, is strongly influenced by the ridge. The ridge is beneath the initial depth of the upper layer that is set at 400 m. Due to the Ekman transport convergence, the layer interface in the center of the gyre is about 620 m below surface, which is also below the ridge that has a depth of 600 m (Figure 9c). We have also conducted another experiment that has a ridge depth at 2000 m (not shown). The ridge still exerts an influence on the upper layer that is qualitatively similar to that shown in Figure 9c. So topographic features, such as ridges, could substitute, to some extents, the dynamical role of a western boundary. The second experiment is with a ridge that extends across the basin (Figure 9b). The ridge segregates the gyres into two roughly symmetric mean cells. It again illustrates how a subsurface ridge can exert a powerful impact on the upper layer circulation.

3.5. Frictional Effects of a Western Boundary

As discussed in the previous section, the insertion of the interior boundary allows the return flow that balances the convergence of the surface Ekman layer transport. Without this boundary, the gyre continues to

strengthen until the circulation becomes unstable baroclinically and eddies are formed. The residual eddy transport becomes a main mechanism to balance the Ekman transport convergence if there is no boundary (see part 2 of this paper in *Yang et al*. [2015]). Another important role of the western boundary is to provide a large torque of friction, due to a narrow boundary current, to balance the vorticity flux from wind stress. This important role is not included in all experiments that have been discussed so far. The boundary, including the inserted one in Figure 7a, has a width of 125 km. This width is considerably larger than a typical width of a frictional western boundary current. The boundary current in all experiments seems to have the same width as the width of the slope. So the magnitude of the frictional torque is probably not as great as what is expected from a frictional western boundary current.

The model uses a biharmonic lateral friction, and the width of the Munk boundary layer is

$$L_{WBC} = \left(\frac{A}{\beta}\right)^{1/5} \tag{4}$$

We used $A = 10^{11}$ m^4 s^{-1} in all four experiments discussed above, so L_{WBC}, according to (4), is about 34.7 km at 85°N and about 22.5 km at 40°N, both are much shorter than 125 km, the width of the slope. So the friction that is exerted along the inserted boundary is considerably weaker than what is expected from the classic Munk or Stommel model [*Munk*, 1950; *Stommel*, 1948].

4. Summary

In this study, we use an idealized model to investigate several parameters and processes that are different from a typical moderate-latitude wind-driven gyre. In an idealized circular basin without a western boundary, the planetary β has a rather small impact on the mean circulation in the upper layer. The mean state of the gyre, measured by the distribution of the upper layer thickness h_1, is similar to that in the control run when β's value is reset from 85°N to 40°N. A small change near the basin's center is probably due to the distribution of closed geostrophic contours in the interior where h_1 is nearly flat and so the geostrophic contours are more sensitive to even a small changes in planetary vorticity *f*. The gyre is more sensitive to the existence of a western boundary. The time-mean circulation in the upper layer weakens considerably when a boundary is inserted between the center and the rim. The boundary provides a route for shoreward return flow to balance the offshore Ekman transport. The role of the planetary β is also elevated when a western boundary is present. The time-mean circulation becomes much more sensitive to the value of the planetary β. We also conducted additional experiments that use a circular basin with subsurface ridges. It is found that ridges exert considerable influences on the upper layer and could substitute to some extents the dynamical role of a western boundary.

Our analyses of vorticity balances have shown that eddies generated by our eddy-permitting model play an important role in the BG dynamics. In particularly, the change of vorticity in the interior is mainly due to eddy flux of vorticity as shown in Figure 4. For the time-mean PV balance, the wind stress curl is mainly balanced by the time-mean divergence of eddy vorticity flux in the interior, and by frictional torque along the boundary (Figure 5). This is different from a typical midlatitude gyre where the main balance is between the wind stress curl and the planetary vorticity advection in the interior, and between friction and vorticity advection along the western boundary. These findings show that dynamics of eddies has been significantly underestimated in the previous studies explaining BG dynamics [*Proshutinsky et al*., 2002, 2009] based only on the variability and strength of the wind stresses and sea ice parameters. More detailed analyses of the role of eddies in BG dynamics and its ability to accumulate and release freshwater from the BG freshwater reservoir will be discussed in the second part of this paper [*Yang et al*., 2015].

Acknowledgments

This study has been supported by the National Science Foundation's Arctic Natural Science Program for J.Y. and A.P. via grant PRL-1107412, and for AP via grants PRL-1313614, PRL-1302884, and PRL-1107277. All simulated data used for our analyses presented in this paper are available by request from Jiayan Yang <jyang@whoi.edu>.

References

Aaboe, S. and O. A. Nøst (2008), A Diagnostic Model of the Nordic Seas and Arctic Ocean Circulation: Quantifying the Effects of a Variable Bottom Density along a Sloping Topography, *J. Phys. Oceanogr.*, *38*, 2685–2703.

Anderson, D. L. T., and A. E. Gill (1975), Spin-up of a stratified ocean, with applications to upwelling, *Deep Sea Res. Oceanogr. Abstr.*, *22*, 583–596.

Curry, R., and C. Mauritzen (2005), Dilution of the northern North Atlantic in recent decades, *Science*, *308*, 1772–1774.

Davis, P. E. D., C. Lique, and H. L. Johnson (2014), On the link between Arctic sea ice decline and the freshwater content of the Beaufort Gyre: Insights from a simplified process model, *J. Clim.*, *27*, 8170–8184, doi:10.1175/JCLI-D-14-00090.1.

Dickson, R. R., J. Meincke, S.-A. Malmberg, and A. J. Lee (1988), The "Great Salinity Anomaly" in the northern North Atlantic 1968–1982, *Prog. Oceanogr.*, *20*, 103–151.
Giles, K. A., S. W. Laxon, A. L. Ridout, D. J. Wingham, and S. Bacon (2012), Western Arctic Ocean freshwater storage increased by wind-driven spin-up of the Beaufort Gyre, *Nat. Geosci.*, *5*, 194–197, doi:10.1038/NGEO1379.
Karcher, M., F. Kauker, R. Gerdes, E. Hunke, and J. Zhang (2007), On the dynamics of Atlantic water circulation in the Arctic Ocean, *J. Geophys. Res.*, *112*, C04S02, doi:10.1029/2006JC003630.
Lique, C., H. L. Johnson, and P. E. D. Davis (2015), On the interplay between the circulation in the surface and the intermediate layers of the Arctic Ocean, *J. Phys. Oceanogr.*, *45*, 1393–1409, doi:10.1175/JPO-D-14-0183.1.
Luneva, M. V., A. J. Willmott, and M. A. M. Maqueda (2012), Geostrophic adjustment problems in a polar basin, *Atmos. Ocean*, *50*(2), 134–155, doi:10.1080/07055900.2012.659719.
Marshall, J., and T. Radko (2003), Residual-mean solutions for Antarctic Circunpolar Current and its associated overturning circulation, *J. Phys. Oceanogr.*, *33*, 2341–2354.
Marshall, J., H. Jones, R. Karsten, and R. Wardle (2002), Can eddies set ocean stratification?, *J. Phys. Oceanogr.*, *32*, 26–38.
McPhee, M. G. (2013), Intensification of geostrophic currents in the Canada Basin, Arctic Ocean, *J. Clim.*, *26*, 3130–3138.
McPhee, M. G., A. Proshutinsky, J. H. Morison, M. Steele, and M. B. Alkire (2009), Rapid change in freshwater content of the Arctic Ocean, *Geophys. Res. Lett.*, *36*, L10602, doi:10.1029/2009GL037525.
Morison, J., R. Kwok, C. Peralta-Ferriz, M. Alkire, I. Rigor, R. Andersen, and M. Steele (2012), Changing Arctic Ocean freshwater pathways, *Nature*, *481*, 66–70, doi:10.1038/nature10705.
Munday, D. R., H. L. Johnson, and D. P. Marshall (2013), Eddy saturation of equilibrated circumpolar currents, *J. Phys. Oceanogr.*, *43*, 507–532.
Munk, W. H. (1950), On the wind-driven ocean circulation, *J. Meteorol.*, *7*, 79–93.
Nøst, O. A., and P. E Isachsen (2003), The large-scale time-mean ocean circulation in the Nordic Seas and Arctic Ocean estimated from simplified dynamics, *J. Mar. Res.*, *61*, 175–210.
Proshutinsky, A., R. H. Bourke, and F. A. McLaughlin (2002), The role of the Beaufort Gyre in Arctic climate variability: Seasonal to decadal climate scales, *Geophys. Res. Lett.*, *29*(23), 2100, doi:10.1029/2002GL015847.
Proshutinsky, A., R. Krishfield, M.-L. Timmermans, J. Toole, E. Carmack, F. McLaughlin, S. Zimmerman, M. Itoh, and K. Shimada (2009), Beaufort Gyre freshwater reservoir: State and variability from observations, *J. Geophys. Res.*, *114*, C00A10, doi:10.1029/2008JC005104.
Proshutinsky, A., et al. (2011), Recent advances in Arctic Ocean studies employing models from the Arctic Ocean Model Intercomparison Project, *Oceanography*, *24*, 102–113, doi:10.5670/oceanog.2011.61.
Proshutinsky, A., R. Krishfield, M.-L. Timmermans, and J. Toole (2013), Arctic Ocean freshwater balance, McGraw-Hill's Yearbook of Science & Technology 2013, McGraw-Hill Education, 448 pp., N. Y.
Spall, M. A. (2013), On the circulation of Atlantic water in the Arctic Ocean, *J. Phys. Oceanogr.*, *43*, 2352–2371, doi:10.1175/JPO-D-13-079.1.
Stommel, H. (1948), The westward intensification of wind-driven ocean currents, *Eos Trans. AGU*, *29*, 202–206.
Timokhov, L. A. and F. Tanis (1997), Environmental Working Group Joint U.S.-Russian Atlas of the Arctic Ocean, National Snow and Ice Data Center, Boulder, Colo., doi:10.7265/N5H12ZX4.
Vallis, G. K. (2006), *Atmospheric and Oceanic Fluid Dynamics: Fundamentals and Large-scale Circulation*, 745 pp., Cambridge Univ. Press, Cambridge, U. K.
Yang, J. (2005), The Arctic and Subarctic Ocean flux of potential vorticity and the Arctic Ocean circulation, *J. Phys. Oceanogr.*, *35*, 2387–2407.
Yang, J. (2006), The seasonal variability of the Arctic Ocean Ekman transport and its role in the mixed layer heat and salt fluxes, *J. Clim.*, *19*, 5366–5387.
Yang, J. (2009), Seasonal and interannual variability of downwelling in the Beaufort Sea, *J. Geophys. Res.*, *114*, C00A14, doi:10.1029/2008JC005084.
Yang, J. (2015), Local and remote wind stress forcing of the seasonal variability of the Atlantic Meridional Overturning Circulation (AMOC) transport at 26.5°N, *J. Geophys. Res. Oceans*, *120*, 2488–2503, doi:10.1002/2014JC010317.
Yang, J., and L. J. Pratt (2013), On the effective capacity of dense-water reservoir for the Nordic Seas overflow: Some effects of topography and wind stress, *J. Phys. Oceanogr.*, *43*, 418–431.
Yang, J., and L. J. Pratt (2014), Some dynamical constraints on upstream pathways of the Denmark Strait Overflow, *J. Phys. Oceanogr.*, *44*, 3033–3053.
Yang, J., A. Proshutinsky, and X. Lin (2015), The dynamics of an idealized Beaufort Gyre, Part 2: The role of Eddies, *J. Geophys. Res.*, in revision.
Zhao, M., M.-L. Timmermans, S. Cole, R. Krishfield, A. Proshutinsky, and J. Toole (2014), Characterizing the eddy field in the Arctic Ocean halocline, *J. Geophys. Res. Oceans*, *119*, 8800–8817, doi:10.1002/2014JC010488.